RESEARCH ARTICLE

NANO · MICRO small
www.small-journal.com

Femtosecond Laser-Induced Nanostructured Sacrificial Layer for Stable Zinc Metal Anode

Sitian Lian, Bo Mai, Zhijun Cai, Yunfan Yue, Zhongle Zeng, Kesong Yu, Xuewen Wang, and Liqiang Mai**

Aqueous zinc-ion batteries are a promising option for grid-scale energy storage owing to their cost-effectiveness and safety. The Zn metal anode with large gravimetric capacity and moderate redox potential can enable high-energy-density Zn batteries. However, the surface instability of commercial Zn metal foils leads to capacity degradation and limited cycle life of batteries. Here, a sacrificial layer strategy is proposed to address these issues by femtosecond laser-induced nanostructuring on the Zn metal substrate (Fs-Zn). This sacrificial layer features an orderly interface consisting of exposed aligned crystal edges after the initial stripping process. This structure induces nearly (101)-oriented epitaxial growth and offers more active sites during the Zn plating/stripping process, effectively minimizing dendrite growth and side reactions. Accordingly, compared with commercial Zn metal, the Fs-Zn symmetric cell shows prolonged operational life, operating for over 500 h at 1 mA cm^{-2}/1 mA h cm^{-2} and 180 h at 0.5 mA cm^{-2}/1.5 mA h cm^{-2}. Moreover, the Fs-Zn||MnO_2 full cell exhibits enhanced cycling stability over 500 cycles. This femtosecond laser-induced sacrificial layer strategy offers an effective solution to the practical application of aqueous zinc-ion batteries.

1. Introduction

Electrochemical energy storage technologies, such as commercial lithium-ion batteries (LIBs), are vital for society as a low-carbon power supply system by reducing fossil-fuel dependence and integrating renewable resources.[1–3] However, the flammable electrolyte and costly lithium resource of LIBs pose new demands on battery development. Notably, aqueous zinc-ion batteries (AZIBs) offer an appealing alternative solution for large-scale renewable energy storage due to their high energy density, safety, and low cost. Moreover, the electrochemical performance of AZIBs is directly related to the Zn metal anode, which is based on the Zn/Zn^{2+} redox couple that has a gravimetric capacity of 820 mAh g^{-1} and an equilibrium potential of −0.76 V versus standard hydrogen electrode.

The production of commercial-grade zinc metal foil involves smelting pure zinc metal, followed by die casting, and then rolling processes to form a thin and lustrous foil without any more surface polishing treatment (**Figure 1a**).[4–6] Therefore, lots of surface random imperfections (fold, crack, scratch, grain boundaries (GBs)) are introduced during the manufacturing process (Figure 1c–e). These irregular and non-planar defective morphologies lead to localized high currents that are susceptible to uncontrollable dendrite growth and parasitic side reactions like hydrogen evolution reduction (HER).[7–10] Worse still, dendrite and side reactions can mutually amplify each other during the cycling process.[11] Consequently, dendrite propagation leads to internal short-circuits by penetrating the separator and the side reactions induce an increase in polarization overpotential and a reduction in capacity, which pose a hurdle to achieving both long-term cyclability and high capacity density in AZIBs.[12]

Constructing the artificial protective layer on the surface of Zn foil is identified as an effective method to optimize the electric field distribution.[13–17] However, researchers have noted that the overlays can block ion transport dynamics for surface redox and often encounter structural nonuniformity and mechanical weakness, resulting in elevated overpotential and coating failure. Therefore, the surface morphology reconstruction strategy via mechanical grinding (surface sandpaper polishing,)[6] chemical etching/polishing (dilute hydrochloric acid etching,[18] Sodium hexametaphosphate chemical polishing,)[19] laser fabrication (femtosecond laser-induced periodic micro/nano structures,[20] and picosecond laser lithography)[21] etc., has already been applied to construct a fresh surface of zinc anode. These surface engineering techniques significantly homogenize the electric field

S. Lian, B. Mai, Z. Cai, Y. Yue, Z. Zeng, K. Yu, X. Wang, L. Mai
State Key Laboratory of Advanced Technology for Materials Synthesis and Processing
Wuhan University of Technology
Wuhan 430070, P. R. China
E-mail: xwwang@whut.edu.cn; mlq518@whut.edu.cn
Z. Cai
Department of Physics
The Chinese University of Hong Kong
Shatin, New Territories, Hong Kong 999077, P. R. China
Y. Yue, Z. Zeng, X. Wang
Center of Femtosecond Laser Manufacturing for Advanced Materials and Devices
State Key Laboratory of Advanced Technology for Materials Synthesis and Processing
Wuhan University of Technology
Wuhan 430070, P. R. China

The ORCID identification number(s) for the author(s) of this article can be found under https://doi.org/10.1002/smll.202505751

DOI: 10.1002/smll.202505751

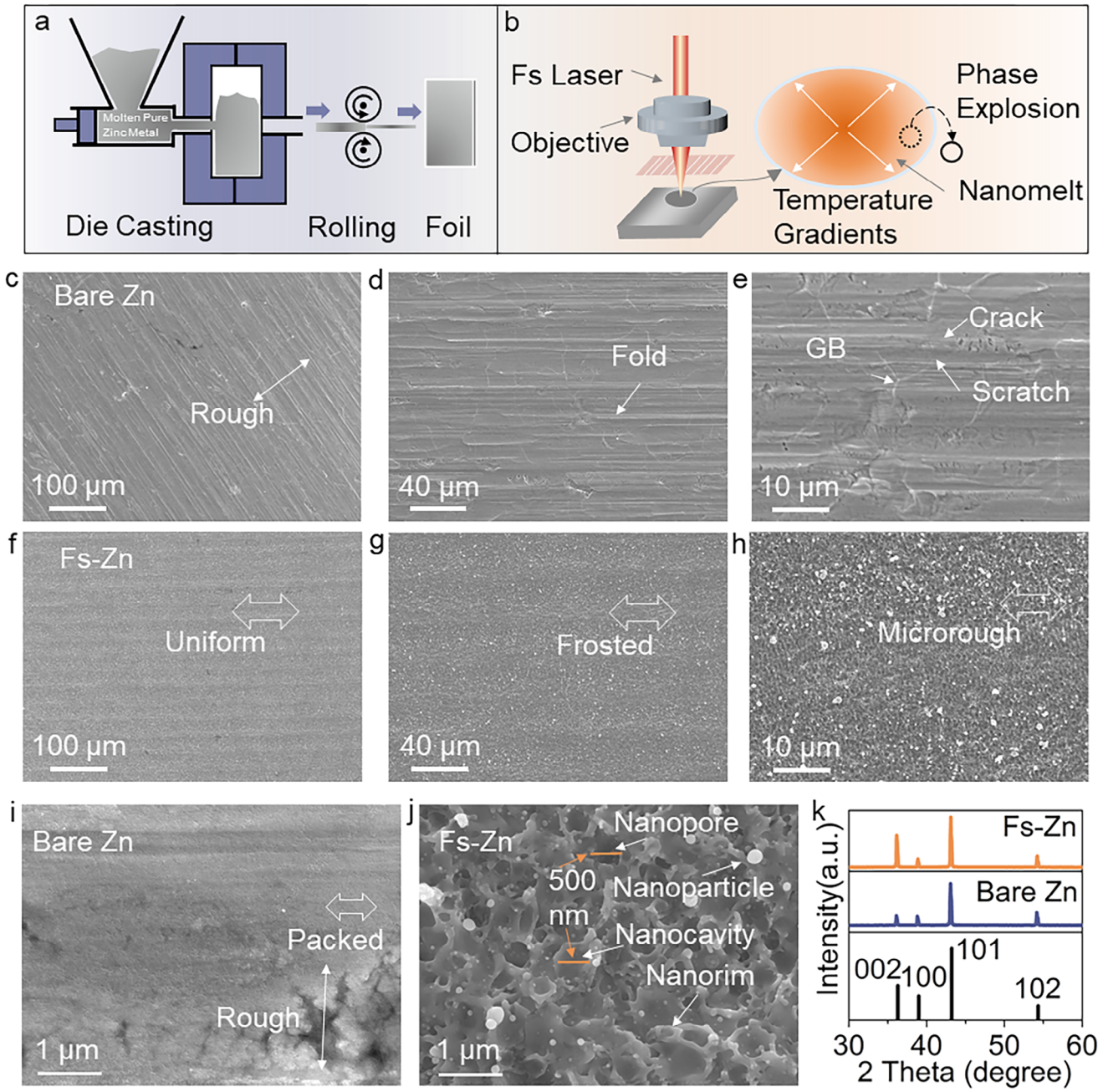

Figure 1. a) Schematic of the production of commercial-grade zinc metal foil. b) The femtosecond laser system (left) and principle diagram of femtosecond laser-induced nanostructuring on Zn (right). c–e,i) SEM images at sequential magnifications of bare Zn; f–h,j) SEM images at sequential magnifications of Fs-Zn. All scale bars in the SEM images are set to an identical length. k) the XRD patterns of bare Zn and Fs-Zn with standard PDF card for Zn(00-004-0831) in the 2θ range from 30° to 60°.

of the Zn anode by regularizing the surface, and increase the Zn ion transport kinetics by exposing more active sites. However, the mechanical stress generated by polishing induces plastic deformation within the Zn metal foil. Additionally, the reliance on manual operation gives rise to substandard repeatability and uneven surface uniformity. Immersion of the Zn foil in a solution readily causes penetration, thereby resulting in damage to mechanical strength and the presence of chemical residues. The non-contact ultrafast laser surface processing technology can effectively solve these issues. Femtosecond laser ablation, characterized by short pulse duration (10^{-15} s) and minimal thermal effects (electron energy relaxation time: 10^{-10}–10^{-12} s)[22] that ensure the fabrication of micro/nano structures, represents a highly promising approach. However, femtosecond laser-induced micro/nano structures lead to new delamination between the fabricated structures and the substrate, resulting in problems similar to those encountered with protective layers. The comparative advantages and limitations of these processing

methodologies are systematically summarized in Table S2 (Supporting Information).

To address the limitations of the artificial protective layer while preserving the merits of the surface morphology reconstruction strategy, a sacrificial layer strategy is proposed. The sacrificial layer is fabricated via femtosecond laser-induced surface nanostructuring of the Zn metal substrate (Fs-Zn). After the initial stripping process, the sacrificial layer exhibits more exposed crystal edges and an orderly interface. These exposed crystal edges provide additional sites for ion adsorption and transfer, while the orderly interface promotes uniform ion distribution. In the subsequent Zn plating/stripping process, the formation of additional active sites and a uniform reaction surface enhance ion-transport kinetics and homogenize ion flux distribution. As a result, the uniform deposition and dissolution of zinc ions are facilitated, effectively minimizing dendrite growth and side reactions. Consequently, the symmetric and full cells assisted by the Fs-Zn anode display better electrochemical performance when compared with bare Zn. Under a current density of 1 mA cm^{-2} and an areal capacity of 1 mAh cm^{-2}, the Fs-Zn symmetric cell operates for over 500 h, which is almost ten times longer than that of bare Zn. Moreover, the Fs-Zn symmetric cell demonstrates a long-term cycle time over 180 h at a low rate with a current density of 0.5 mA cm^{-2} and an areal capacity of 1.5 mAh cm^{-2}, and bare Zn abruptly fails under those conditions due to the chemical side reactions. Additionally, the Fs-Zn||MnO_2 full cell can complete 500 cycles with a higher specific capacity compared with the bare Zn||MnO_2 full cell. This femtosecond laser-induced nanostructured sacrificial layer strategy is highly appealing for large-scale industrial production and paves the way for the widespread adoption of aqueous zinc-ion batteries in various applications.

2. Results and Discussion

2.1. Formation and Characterization of Fs-Zn

The experimental setup for femtosecond laser-induced nanostructuring on Zn is schematized in Figure 1b (left). The femtosecond laser system performs surface scanning on commercial zinc foils along parallel paths. The key laser parameters and their effects on nanostructure morphology are systematically summarized in Table S1 (Supporting Information). These parameters enable precise control over the surface oxidation state, surface texture, and micro/nano-features, regulating both the surface density and spatial distribution of electrochemically active sites.[12,23] Scanning electron microscopy (SEM) image in Figure 1f shows a frosted surface of Fs-Zn with slight processing traces. Meanwhile, the bare Zn in Figure 1c shows a rough surface. In the following SEM images at sequential magnifications, Fs-Zn exhibits different microstructural features compared to bare Zn. Significantly, Figure 1g reveals a uniform topography of Fs-Zn, in contrast to the bare Zn (Figure 1d) which displays prominent fold lines. In Figure 1h, the surface of Fs-Zn is marked by microroughness along with sparsely distributed dominant grains. Whereas distinct scratch patterns, cracks, and GBs prevail on the bare Zn surface in Figure 1e. The droplet sputtering-like morphology of Fs-Zn, with a feature size as small as ≈500 nm, is depicted in Figure 1j. It exhibits micro-holes with sunken structures and some randomly distributed nanoparticles. Notably, the microstructure of Fs-Zn is composed of features like nanopores, nanoparticles, nanocavities, and nanorims. Meanwhile, the bare Zn exhibits a densely packed yet rough surface (Figure 1i). Therefore, the femtosecond laser processing generates a hierarchically structured surface on top of the zinc substrate. This engineered nanostructured surface features a complex topography (nanopores, nanocavities, nanorims, nanoparticles) distinct from the internal bulk zinc substrate. This engineered surface layer could alter the interfacial properties compared to the bare Zn. The corresponding cross-sectional SEM analysis of the post-processed material reveals distinctive depth-related features, showing a bulk thickness reduction of ≈3 µm relative to the as-prepared state along with characteristic surface topography formed by nanocavities with depths of ≈300 nm (Figure S1, Supporting Information). Energy dispersive X-ray spectroscopy (EDS) surface and point analyses were conducted to identify the oxidation degree of Zn foil before and after femtosecond laser treatment (Figure S2, Supporting Information). The quantitative analyses in the surface region (Table S3, Supporting Information) show that the oxygen concentration of the bare Zn foil (≈9.91 at.%) decreased to ≈6.02 at.% on the Fs-Zn anode after treatment. EDS point analysis reveals that the nanoparticle contains a small amount of oxygen (≈3.97 at.%), demonstrating that it is a zinc metal-rich particle. The attenuated total reflection Fourier transform infrared (ATR-FTIR) spectra of bare Zn (matched with $Zn(OH)_2$ and Fs-Zn (matched with $ZnO{\cdot}H_2O$, surface-adsorbed water) are shown in Figure S3 Supporting Information).[24] In the bare Zn spectrum, broad bands are observed at 3000–3600 cm^{-1} (O-H stretching modes), 800–1200 cm^{-1} (Zn-OH bending modes), and 450–800 cm^{-1} (Zn-O stretching modes). In contrast, the Fs-Zn spectrum exhibits broad bands only in the ranges of 800–1200 cm^{-1} and 450–800 cm^{-1}, with a blue shift in wavenumbers indicating weaker hydrogen bonding due to the presence of crystalline water (H_2O). These results suggest that femtosecond laser processing removes the $Zn(OH)_2$ passivation layer present on bare Zn, which otherwise hinders electron transport and Zn deposition.[25]

The formation mechanism of the morphology of Fs-Zn is schematized in Figure 1b (right). The morphological evolution of Fs-Zn involves femtosecond laser-induced local melting and phase explosion processes:[26–28] 1) These two processes occur on the same time scale and are intricately intertwined with one another; 2) At the incident laser fluence approaches the laser ablation threshold, the spatial energy deposition non-uniformities generate localized melt nanoscale pools, where steep radial temperature gradients drive Marangoni flows. At this stage, a high radial temperature gradient in the nanomelt induces a radial surface tension gradient, pushing the liquid to the periphery of the nanomelt. At the boundary with the solid-state material, the expelled liquid solidifies rapidly, resulting in the formation of nanocavities, nano protrusions, and nanorims; 3) When the laser fluence is high enough to induce ablation, the atoms ejected from the nanomelts generate a recoil pressure. This recoil pressure triggers a phase explosion, which causes the liquid metal to be ejected in the form of micro-jets, resulting in the formation of nanoscale droplets. As these droplets cool down, they solidify into monodisperse nanoparticles; 4) In conclusion, during the scanning of the zinc foil surface by a femtosecond laser at fluences close to the ablation threshold, microstructures

including nanopores, nanocavities, and nanorims are formed. Subsequently, owing to the energy accumulation induced by the different surface states of zinc, ablation occurs, and consequently, some nanoparticles are formed on the surface of Fs-Zn.

The X-ray diffraction (XRD) results show that the femtosecond laser-induced nanostructuring process on Zn can enhance the intensity of Zn(002) crystal plane (Figure 1k). This result suggests that during the process of high-energy laser pulses interacting with the zinc surface, the formation of the (002) basal plane in Fs-Zn is promoted. The prevalence of the (002) basal plane associated with the lower surface energy thermodynamically contributes to maintaining a uniform stripping/plating process.[29,30] Interestingly, the proportion of the (101) diffraction peak in bare Zn is consistently higher than that in Fs-Zn, likely due to the consumption of (101) crystal planes during the fabrication of the sacrificial layer.

2.2. Verification and Positive Role of the Sacrificial Layer in Fs-Zn

The verification of the sacrificial layer in Fs-Zn is performed by analyzing the morphology features of the stripped Zn electrodes through SEM images. The necessity of the stripping process is that it is the initial step in a typical discharge-and-charge test of aqueous zinc-ion batteries.[31] During the stripping process of Fs-Zn, as the capacity increases, an increasing number of aligned crystalline edges are exposed. Upon stripping with a capacity of 0.1 mAh cm^{-2}, the surface, which initially features a nanostructured layer (**Figure 2a**), evolves into a textured structure (Figure 2b). In the high-magnification SEM images, nanostructures like the nanopores, nanocavities, and nanorims existing in the original Fs-Zn (Figure S4a, Supporting Information) partially disappear, and aligned crystalline edges of the Zn substrate appear (Figure S4b, Supporting Information). Following the stripping with 0.5 mAh cm^{-2}, distinct crystalline edges are observable in the low-magnification SEM image (Figure 2c), indicating a more extensively exposed crystalline surface. Combining high-magnification SEM images (Figure S4c, Supporting Information), the results confirm varying degrees of the stripped state. In certain regions, a great number of crystal planes of the structure are exposed, characterized by a large interplanar spacing, a loose structure, and well-defined crystal-plane boundaries; conversely, in other regions, fewer crystal planes are exposed, with a small interplanar spacing, a compact structure, and blurred boundaries. This may be derived from the varying surface energies of zinc crystal planes.[32,33] After stripping with a capacity of 1 mAh cm^{-2}, the stripped surface shows large-scale densely-packed edges with a uniform planar structure (Figure 2d), signifying the complete exposure of the crystal planes of the Zn substrate. Furthermore, high-magnification SEM images clearly reveal distinct crystal-plane boundaries (Figure S4d, Supporting Information), indicating the disappearance of the nanostructured layer. Additionally, these aligned crystalline edges are covered with uniformly generated zinc hydroxide sulfate (ZHS) hexagonal flakes, which are expected to alleviate subsequent side effects.[17] In contrast, the SEM images reveal inhomogeneous void spaces (Figure 2f–h; Figure S4f—h, Supporting Information) formed on the surface of bare Zn due to the nonuniform dissolution resulting from the rough surface (Figure 2e; Figure S4e, Supporting Information). Moreover, the void space and packed plane on the surface of bare Zn exhibit localized bulk stripping from the initial defective surface. The effect of the nanostructures of the sacrificial layer during the Zn plating process is shown in Figures S5 and S11 (Supporting Information). The nanostructures in Fs-Zn provide more active sites for Zn deposition, thereby reducing the occurrence of large and compact protrusions.

Ex situ and in situ, XRD analyses were conducted to mainly investigate the structure of crystalline surfaces during the sacrificial layer stripping process. The ex situ XRD results (Figure 2i) demonstrate that during the Zn stripping process, the intensity of the characteristic peak of ZHS at ≈8.5° exhibits significant differences between the Fs-Zn electrodes and bare Zn electrodes. Specifically, the intensity of this peak on the surface of the Fs-Zn electrodes is significantly lower than that of bare Zn electrodes, indicating a diminished content of ZHS by-products in the Fs-Zn electrodes, which suggests that the side reactions occurring in the Fs-Zn electrodes are alleviated.[34] Similar results were observed during the Zn plating process (Figure S6, Supporting Information). In-situ XRD patterns (Figure 2j; Figure S7, Supporting Information) reveal that during the discharge process, the intensity of the (002) diffraction peak of electrodes decreases, while that of the (100) diffraction peak increases. This indicates that the Zn(002) plane is consumed in the stripping process and the Zn(100) plane is exposed, suggesting that vertically-oriented Zn forms,[35] which is consistent with the SEM results (Figure S4, Supporting Information). Additionally, although the (101) diffraction peak in bare Zn shows negligible variation, the (101) diffraction peak in Fs-Zn gradually shifts to a higher angle, indicating a contraction in the lattice spacing of (101) crystal planes induced by the disappearance of the nanostructures in the sacrificial layer.[36–38] The (101) diffraction peak in Fs-Zn shows a significant enhancement compared with Zn(002) and Zn(100) diffraction peaks, suggesting that near-vertical alignment forms,[33] which is consistent with the SEM results (Figure 2b–d, Figure S4b–d, Supporting Information). Scanning electron microscope-electron backscatter diffraction (SEM-EBSD) analysis reveals that the crystallographic orientations in the edge predominantly correspond to the (101) planes (Figure S8, Supporting Information).

The influence of the nanostructuring layer on the zinc plating/stripping behavior is further confirmed by the Zn||Zn cell. The initial charge transfer resistance measured by electrochemical impedance spectroscopy (EIS) in the Fs-Zn symmetric cell is lower than that of the bare Zn system (Figure 2k). This decrease in resistance reveals that Fs-Zn has more rapid Zn^{2+} transport kinetics and higher energy efficiency. The voltage profiles (Figure 2l) of galvanostatic Zn deposition at 1 mA cm^{-2} for 1 mAh cm^{-2} show that in the first stripping process, Fs-Zn exhibits a smaller stripping overpotential compared to bare Zn, indicating that Fs-Zn requires less energy to drive the stripping process at the electrode surface.[39] These results can be attributed to the fact that, compared to the bulk stripping in bare Zn foil surface, the stripping of the nanostructured layer in Fs-Zn can provide abundant active sites, which endows Fs-Zn with higher reaction activity.[12,40]

Figure 2m illustrates the mechanism underlying the functional mechanism of the nanostructured sacrificial layer. The surface of Fs-Zn is characterized by numerous nanostructures. These nanostructures increase the number of surface-active sites,

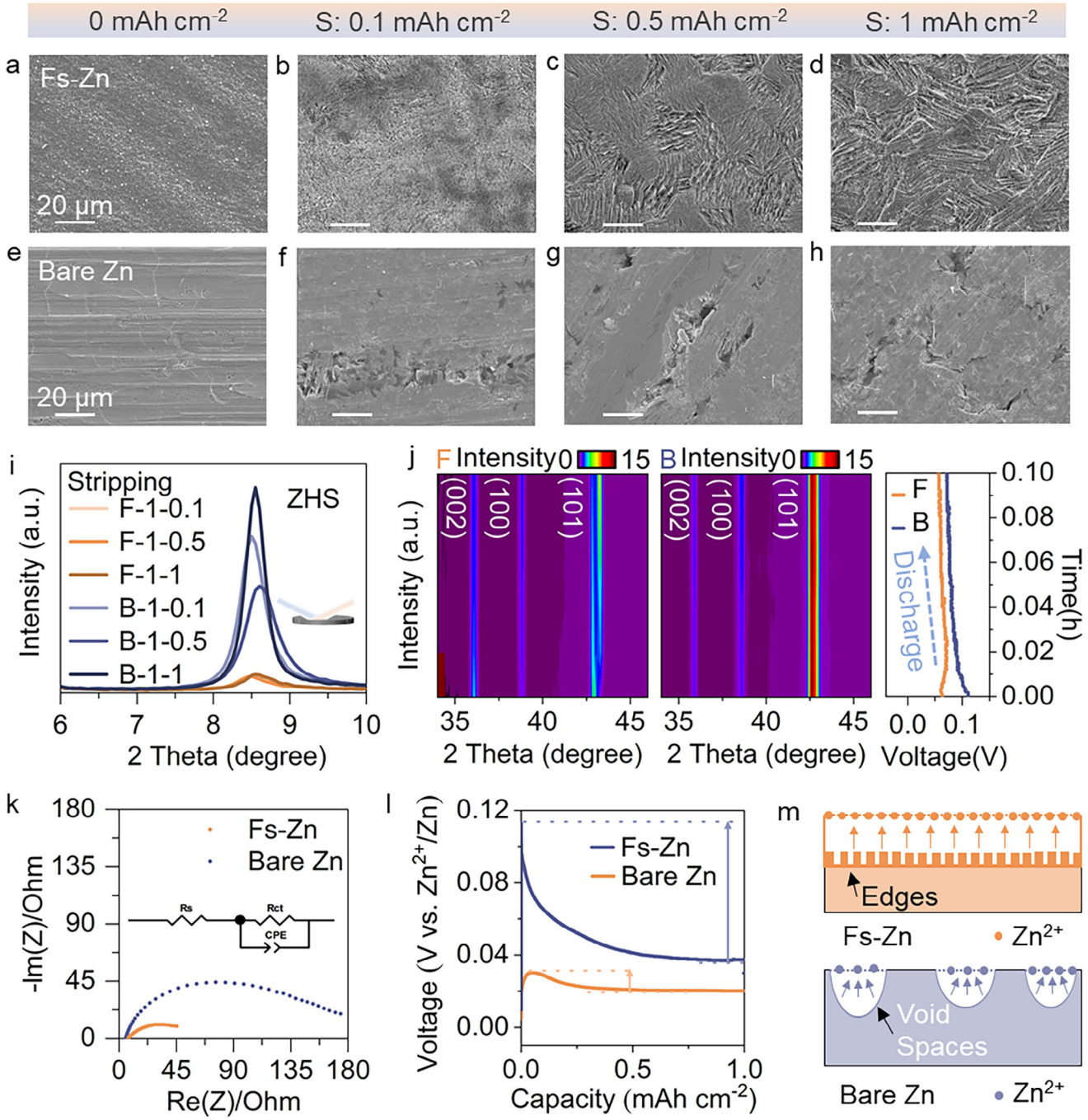

Figure 2. SEM images of a) pristine and stripped (S) Fs-Zn at a current density of 1 mA cm^{-2} with capacities of b) 0.1 mAh cm^{-2}, c) 0.5 mAh cm^{-2}, and d) 1 mAh cm^{-2}, respectively; SEM images of e) pristine and stripped bare Zn at 1 mA cm^{-2} with capacities of f) 0.1 mAh cm^{-2}, g) 0.5 mAh cm^{-2}, and h) 1 mAh cm^{-2}, respectively. All scale bars in these SEM images are set to an identical length. i) Ex situ XRD patterns of Fs-Zn (F) electrode and bare Zn (B) electrode after Zn stripping at capacities of 0.1 mAh cm^{-2}, 0.5 mAh cm^{-2} and 1 mAh cm^{-2} at 1 mA cm^{-2}. All the experiments on ex-situ XRD were uniformly performed on a 10 mm Zn electrode. j) 2D maps of in-situ XRD spectra and corresponding discharge profiles of electrodes with a capacity of 1 mAh cm^{-2} at 6 mA cm^{-2}. k) EIS analysis for pristine Zn||Zn symmetrical cells; l) Voltage profiles of galvanostatic Zn stripping at 1 mA cm^{-2} for 1 mAh cm^{-2}; m) Schematic of the functional mechanism of nanostructures in Fs-Zn foil.

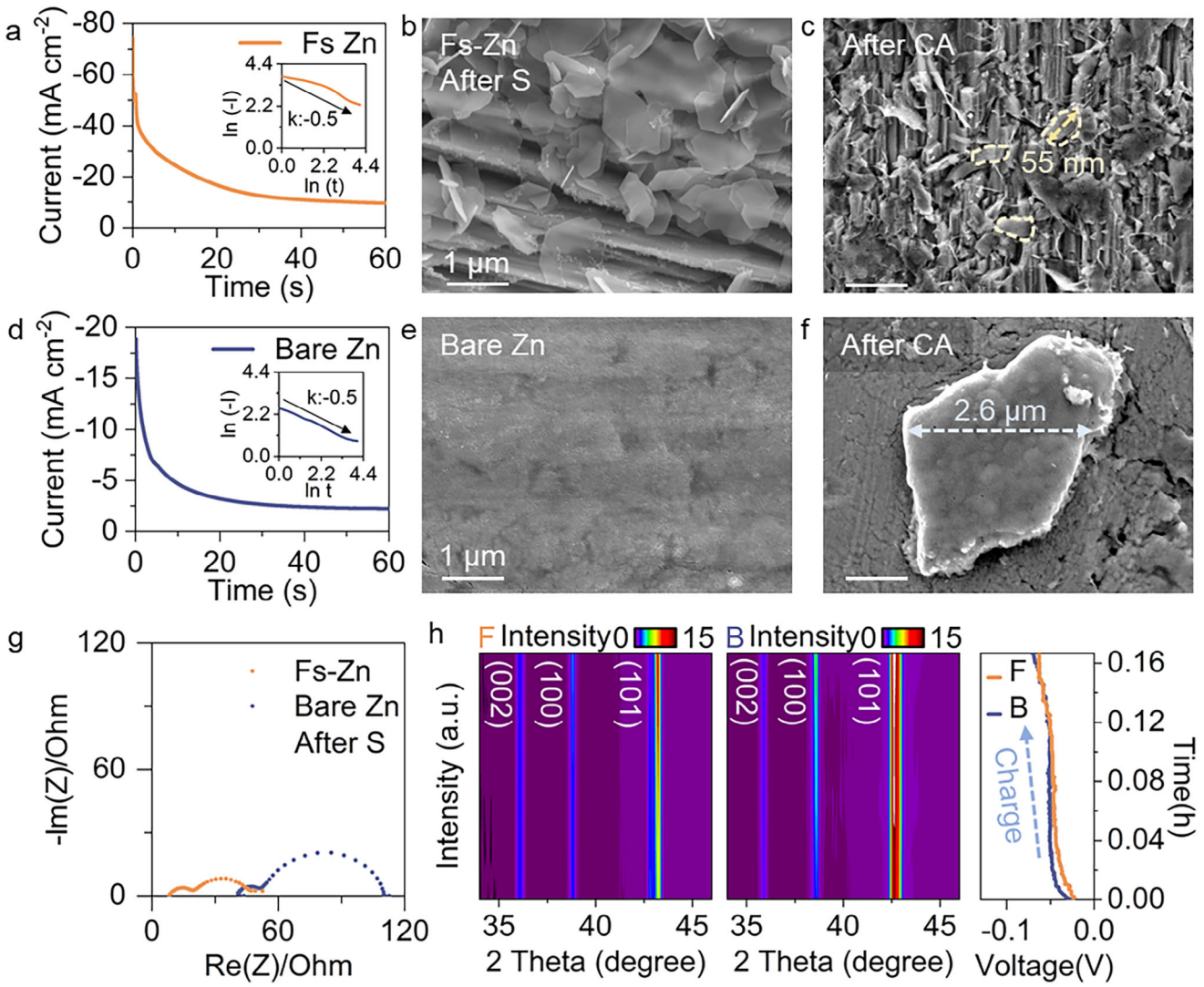

Figure 3. Current transients during Zn depositions on a) Fs-Zn with a pre-stripped capacity of 1mAh cm^{-2} and d) bare Zn obtained at −100 mV versus Zn^{2+}/Zn. The inner curves show the ln (-I)-ln (t) plots for current transients and the arrows show the characteristic slope of −0.5 associated with the Cottrell parameter. SEM images of b) pre-stripped Fs-Zn and c) the final Zn deposits on the pre-stripped Fs-Zn; SEM images of e) bare Zn and f) the final Zn deposits on the bare Zn. All scale bars in these SEM images are set to an identical length. g) EIS analysis of Zn||Zn symmetrical cells with a pre-discharge with a capacity of 1mAh cm^{-2} at 1 mA cm^{-2}. h) 2D maps of in situ XRD spectra and corresponding charge profiles of electrodes with a capacity of 1 mAh cm^{-2} at 6 mA cm^{-2} after first discharge with a capacity of 1 mAh cm^{-2} at 6 mA cm^{-2}.

which serve as favorable sites for Zn^{2+}/Zn oxidation reactions. Additionally, the surface uniformity of Fs-Zn ensures a uniform surface with denser edges after stripping. The newly obtained abundant edges can serve as new active sites for subsequent reactions, which is favorable for enhancing ion-transport kinetics in Fs-Zn. Furthermore, the uniform surface with denser edges can homogenize ion flux. Conversely, bare Zn presents an uneven surface topography with limited reactive sites. During stripping, the non-uniform dissolution of bare Zn leads to localized stripping, generating extensive void formation. This could result in subsequent slow reaction kinetics and non-uniform ion distribution.

The surface state of the substrate exerts a significant influence on the Zn nucleation and growth electrodeposition behavior. This deposition behavior was investigated by current transients (**Figure** 3a,d) through chronoamperometric tests, during which an overpotential of −100 mV was applied to the electrodes in a solution containing 1 M Na_2SO_4 and 0.1 M $ZnSO_4$. During the Zn deposition process, the current decreases with time, which is due to the reduction of the surface concentration of the reactant.[41] The presence of more active sites available for zinc nucleation and growth on the stripped Fs-Zn (Figure 3b) leads to faster reaction kinetics thereby inducing a large current. In contrast, the limited active sites on the bare Zn (Figure 3e) restrict the reaction kinetics, resulting in a smaller current compared to that of Fs-Zn. Cottrell curves are shown on the inner log current versus log time curves.[42,43] The slope close to −0.5 for the bare Zn indicates that its nucleation and growth process is diffusion-controlled under this condition (Figure 3d). For Fs-Zn, the initially large slope implies that the current decreases

more slowly with time (Figure 3a), suggesting that this process is not only governed by diffusion but also affected by the high redox activity surface. Subsequently, the slope approaches −0.5, indicating that the redox reaction on the surface reaches a steady state and the deposition enters a diffusion-controlled stage. Finally, both electrodes reach a diffusion equilibrium state and the current changes minimally with time. It is worth noting that compared with the pronounced protrusions with a characteristic size of 2.6 μm formed on the bare Zn (Figure 3f), the multiple distributed nanograins with a characteristic size of 55 nm on Fs-Zn (Figure 3c) have the advantages of alleviating subsequent corrosion reactions and dendrite growth.

The resistance of the symmetric cells after a pre-discharge with a capacity of 1mAh cm^{-2} at a current density of 1 mA cm^{-2} was measured by EIS (Figure 3g). In the Nyquist plots, compared with the EIS results of pristine electrodes (Figure 2k), a new semicircle at high frequency, which represents the solid electrolyte interphase resistance (R_{SEI})[44,45] appears in the pre-discharged cells. Moreover, the pre-discharged cells have a higher internal resistance (R_s), suggesting that the R_{SEI} and higher R_s may result from the transfer of zinc ions through the ZHS. Meanwhile, the semicircle at medium frequency corresponds to the charge transfer resistance, and the decreased charge transfer resistance in Fs-Zn compared with bare Zn represents the better plating/stripping reversibility of Fs-Zn.[46] These lower resistances may result from the fewer side reaction productions and more active sites on the Fs-Zn. In situ, XRD patterns (Figure 3h; Figure S9, Supporting Information) show that during the charging process, the intensity of the Zn(002), Zn(100), and Zn(101) diffraction peaks increases corresponding to the deposition of zinc.[47] The (101) diffraction peak in Fs-Zn also shows a significant increase compared with Zn(002) and Zn(100) diffraction peaks, indicating the near-vertical oriented Zn deposition with preferential growth of (101) plane,[33] which will be discussed later. In contrast, there is no substantial increase in the diffraction peaks in bare Zn, which can be attributed to the random orientations of the zinc deposition.[35]

The electrochemical performance of Fs-Zn anodes is anticipated to experience substantial improvements. To verify the benefits of the nanostructured sacrificial layer in Zn anodes, plating/stripping measurements were conducted within a symmetrical cell configuration. A thin GF/A separator with a thickness of 260 μm was utilized, as depicted in **Figure 4a**. As predicted, when evaluating the rate performance at an areal capacity of 1 mAh cm^{-2} with current densities ranging from 0.5 mA cm^{-2} to 10 mA cm^{-2}, the Fs-Zn symmetrical cell demonstrates reliable operation up to a current density of 10 mA cm^{-2}. In contrast, the bare Zn suffered an obvious short circuit at 5 mA cm^{-2} (Figure 4b), with internal short circuits being induced by Zn dendrite growth in this condition.[48] Subsequently, constant-current-density charge/discharge analyses were carried out to validate the stability of symmetrical cells over long cycles. Correspondingly, XRD and SEM characterizations during the plating/stripping process were performed to investigate the effects of side reactions and dendrite growth. Figure 4c shows that when the symmetrical cells operate at a low current density of 0.5 mA cm^{-2} with an areal capacity of 1.5 mAh cm^{-2}, which is a low-rate test making the cells susceptible to time-controlled chemical side reactions,[49] the Fs-Zn symmetric cell endures for 180 h, while the bare Zn features a large increase in overpotential of 200 mV and fails rapidly. The associated ex-situ XRD results in Figure 4e demonstrate that after the Zn stripping-plating or plating-stripping process, the intensity of the characteristic peak of ZHS at ≈8.5° on the surface of the bare Zn electrodes is significantly higher than that of Fs-Zn electrodes, indicating an increased content of ZHS by-products in the bare Zn electrodes, which accelerates the failure of the cell. The SEM images present that after the Zn stripping-plating process, Fs-Zn exhibits a subplanar composed of nearly vertically-aligned, packed crystal edges (Figure 4f), while a large dendrite protrusion was plated on the bare Zn (Figure 4g), facilitating the occurrence of the side reactions. After the Zn plating-stripping process, Fs-Zn presents a flat surface constituted of packed crystal edges (Figure 4j), with small and uniform hexagonal ZHS. In contrast, on the bare Zn, large and randomly distributed ZHS by-products occur (Figure 4k), suggesting a longer zinc ion diffusion pathway that affects the ion transfer.[17] Moreover, under a current density of 1 mA cm^{-2} and an areal capacity of 1 mAh cm^{-1}, the Fs-Zn symmetric cell presents a long cycle life, maintaining a stable voltage profile over an operational period exceeding 500 h with a voltage hysteresis of ˂22 mV (Figure 4d). Conversely, the bare Zn symmetric cell shows a voltage hysteresis exceeding 45 mV, followed by an 80 mV increment in overpotential during the cycling process. Subsequently, a voltage drop induced by dendrite formation occurs after 60 h, leading to the failure of the cell. The corresponding ex situ XRD results in Figure 4e reveal that subsequent to the Zn stripping-plating or plating-stripping process, a higher content of ZHS by-products emerges in the bare Zn electrodes which is likely responsible for the elevated overpotential within the cell. The SEM images indicate that after the Zn stripping-plating process, the Fs-Zn features densely packed crystal edges (Figure 4h), resulting in a surface that is more even than the protruding bare Zn surface (Figure 4i). After the Zn plating-stripping process, Fs-Zn presents a uniform stripped surface (Figure 4l). In contrast, on the bare Zn electrode, residual zinc protrusions are randomly left after the stripping process (Figure 4m). This is due to the isolation of Zn during the process,[50] which can affect the reversibility and induce dendrite growth.

In summary, XRD results show that after half cycle (Figure 2i; Figures S6 and S10, Supporting Information) and one cycle (Figure 4e), the intensity of the ZHS peak in Fs-Zn is lower than that in bare Zn, indicating that side reactions in Fs-Zn are significantly alleviated, which is due to the fact that the abundant edges serve as active sites that enhance Zn ion-transport kinetics. SEM analysis reveals that bare Zn electrodes exhibited pronounced dendrite growth, which could be attributed to the non-uniform reaction activity on the surface. In contrast, following the stripping process (Figures 2a–h and 4f-m; Figures S4a–h and S11, Supporting Information), the Fs-Zn electrodes present nearly vertically-aligned, densely packed crystal edges and this structure is maintained during the following plating and stripping process. This morphology homogenizes ion flux, ensuring uniform plating/stripping. When combined with the in situ XRD results (Figures 2j and 3h), it is evident that these aligned crystal edges of the Zn plates correspond to the Zn(101) crystal plane, showing that a nearly (101)-oriented epitaxial growth is induced.[33] Thereby, dendrite growth is effectively suppressed in Fs-Zn electrodes. These results demonstrate that the nanostructured sacrificial layer plays a positive role during the cycle process.

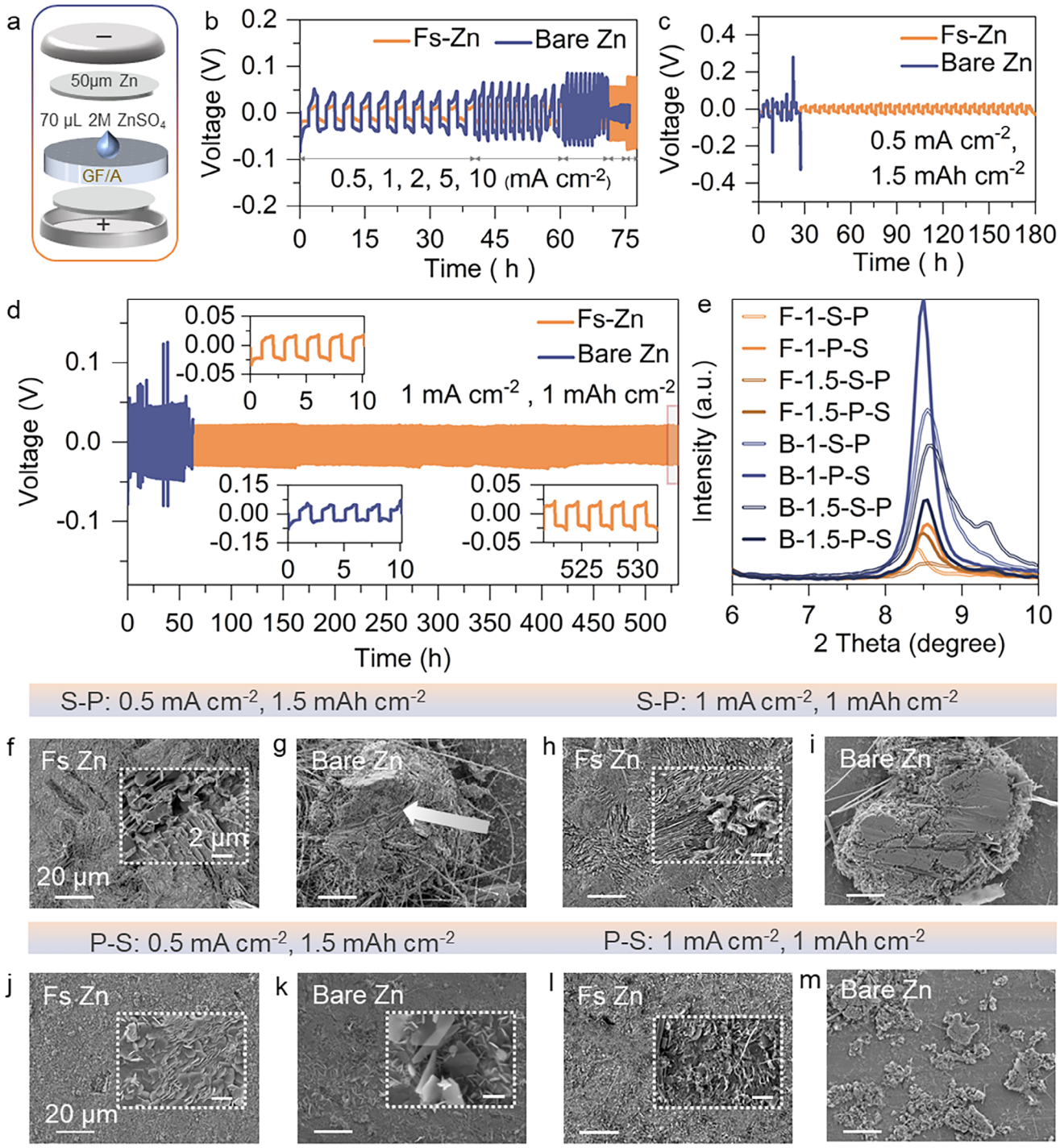

Figure 4. a) The simplified illustration of the Zn||Zn symmetric cell. b) Rate performance of Zn||Zn symmetrical cells at current density/capacity density of 0.5 mA cm^{-2}/1 mAh cm^{-2}, 1 mA cm^{-2}/1 mAh cm^{-2}, 2 mA cm^{-2}/1 mAh cm^{-2}, 5 mA cm^{-2}/1 mAh cm^{-2} and 10 mA cm^{-2}/1 mAh cm^{-2}, respectively; c) Voltage profiles for Zn||Zn symmetric cells at 0.5 mA cm^{-2}/ 1.5 mAh cm^{-2}; d) Voltage profiles for Zn||Zn symmetric cells at 1 mA cm^{-2}/1 mAh cm^{-2}. The insets show the first 5 cycles and the last 5 cycles of the voltage profiles. e) Ex situ XRD patterns of Fs-Zn (F) and bare Zn (B) electrodes after Zn stripping (S)/plating (P) at 1 mA cm^{-2}/1 mAh cm^{-2} (1) and 0.5 mA cm^{-2}/1.5 mA cm^{-2} (1.5). F-1-S-P refers to the ex-situ XRD patterns of the Fs-Zn (F) electrode after Zn stripping (S) followed by plating (P) at 1 mA cm^{-2}/1 mAh cm^{-2} (1). The interpretations of other legends are consistent. All the experiments were uniformly performed on a 10 mm Zn electrode. SEM images of f) Fs-Zn and g) bare Zn electrodes after Zn stripping (S) followed by plating (P) at 0.5 mA cm^{-2}/1.5 mAh cm^{-2}. SEM images of h) Fs-Zn and i) bare Zn electrodes after Zn stripping followed by plating at 1 mA cm^{-2}/1 mAh cm^{-2}. SEM images of j) Fs-Zn and k) bare Zn electrodes after Zn plating followed by stripping at 0.5 mA cm^{-2}/1.5 mAh cm^{-2}. SEM images of l) Fs-Zn and m) bare Zn electrodes after Zn plating followed by stripping at 0.5 mA cm^{-2}/1.5 mAh cm^{-2}. The inner figures are the high-magnification SEM figures. The scale bars in the inner and outer SEM images are set to an identical length, respectively.

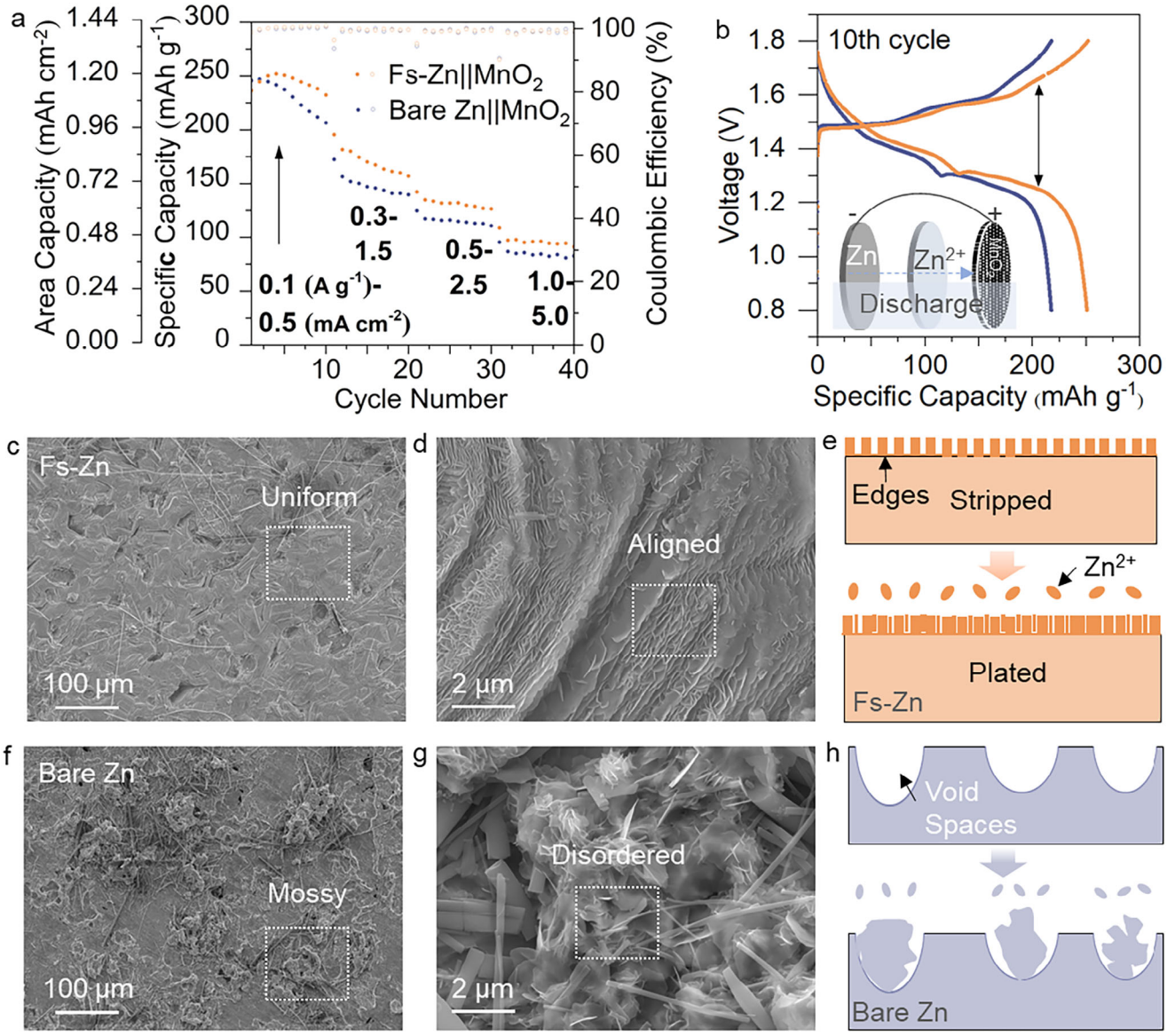

Figure 5. a) Rate performance of Zn||MnO_2 full cells. b) the voltage profiles for the 10th cycle correspond to (a), and the simplified illustration of the Zn||MnO_2 cell during the initial discharge process is inset. c,d) SEM images of the cycled Fs-Zn anode at sequential magnifications after the rate test. f,g) SEM images of cycled bare Zn at sequential magnifications after the rate test. e,h) schematics of the functional mechanism of the morphology evolution for the Fs-Zn anode and the bare Zn anode, respectively. All scale bars in the SEM images are set to an identical length.

2.3. High-Performance Fs-Zn Full Battery with a Sacrificial Layer in the Zn Anode

The electrochemical performance of the Fs-Zn anode was further evaluated in full cells utilizing a MnO_2 cathode. The initial discharge process during full-cell operation is illustrated in the inset in Figure 1b. In the rate performance test (**Figure 5a**), the current density was increased from 0.1 A g^{-1} (0.5 mA cm^{-2}) to 1 A g^{-1} (5 mA cm^{-2}) during the 40 cycles of the stripping-plating process. The anode undergoes complex electrochemical reactions, and Fs-Zn||MnO_2 exhibits a higher specific discharge capacity compared with bare Zn||MnO_2. Additionally, the voltage-capacity plot in the tenth cycle shows that Fs-Zn||MnO_2 displays smaller voltage hysteresis (Figure 5b), suggesting that the Fs-Zn anode features lower energy consumption and higher reversibility of the electrode reaction during the electrochemical process.[51] SEM characterization results reveal the morphology of Fs-Zn and bare Zn anodes after the rate test. Figure 5c shows that the Fs-Zn anode develops a uniform surface after cycling, and its microstructure exhibits a layered structure, featuring relatively ordered, structured growth patterns with aligned textures (Figure 5d). Based on the aforementioned results in Figure 2, this verifies that the crystal edges, originating from the nanostructures acting as a sacrificial layer during the first-cycle stripping, provide a basis for the stable operation of the Fs-Zn||MnO_2 cell during stripping-plating cycles (Figure 5e). These edges effectively inhibit dendrite

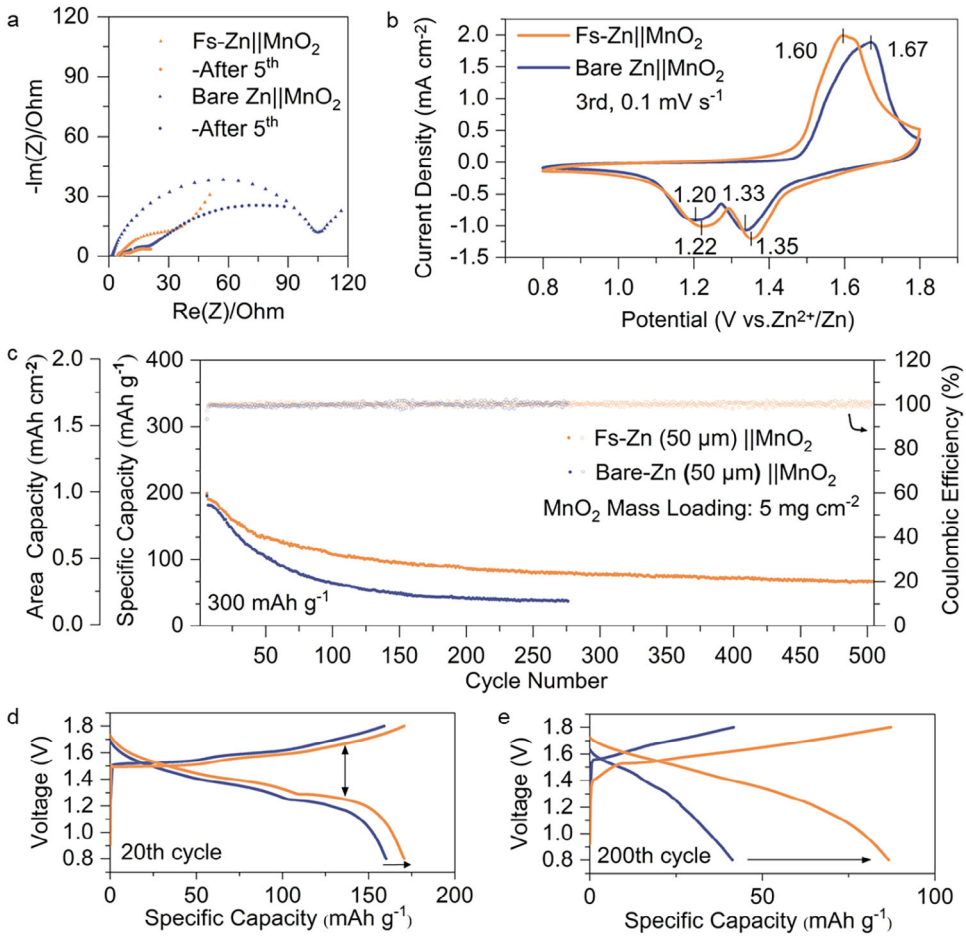

Figure 6. a) EIS plots of Zn||MnO_2 full cells before and after 5 cycles. b) Cyclic voltammetry (CV) plots (3rd) of Zn||MnO_2 full cells at 0.1 mV s^{-1}. c) Cycling performance of Zn||MnO_2 full cells. d)Voltage profiles for the 20th correspond to (c). e) Voltage profiles for the 200th correspond to (c).

growth by enhancing reaction kinetics and optimizing the ion-transport pathway, thereby improving the structural stability of the anode and the electrochemical performance of the battery. In contrast, evident mossy dendritic structures form on the surface of the bare Zn anode (Figure 5f), characterized by a rough surface with disordered protrusions (Figure 5g). Owing to the occurrence of local stripping on the bare Zn anode, the nonuniformity of the electrode provides favorable conditions for the dendrite rapid growth (Figure 5h). This induces side reactions, substantially increasing the internal resistance and hindering the battery capacity release.

EIS analysis (**Figure 6a**) shows that the charge transfer resistance in Fs-Zn||MnO_2 is reduced compared with that in bare Zn||MnO_2 before and after 5 cycles, which supports the improved electrochemical kinetics of the Fs-Zn anode. Compared to the initial state, the charge transfer impedance becomes smaller after cycling, indicating an activation process of the electrode materials.[52] The CV plots (Figure 6b) (3rd) reveal that the Fs-Zn||MnO_2 cell exhibits a lower oxidation peak at 1.60 V (versus 1.67 V for bare Zn||MnO_2), and the higher reductive peaks at 1.35 V (vs. 1.33 V), and 1.22 V (vs. 1.20 V). These results demonstrate that reduced polarization at the Fs-Zn anode contributes to lower initial voltage hysteresis compared with the bare Zn anode.

For long-term cycling (Figure 6c), with a specific current of 0.3 A g^{-1}, Fs-Zn||MnO_2 demonstrates a slightly higher capacity in early cycles. During further cycling, the charge and discharge capacity of bare Zn||MnO_2 deviates gradually. Therefore, Fs-Zn||MnO_2 full cell can achieve 500 cycles with a higher specific capacity. The voltage profiles reveal the voltage hysteresis and capacity change during the cycles. In the 20th cycle, the Fs-Zn||MnO_2 cell shows less voltage hysteresis and higher specific capacity than the bare Zn||MnO_2 cell (Figure 6d), indicating better electrode reaction reversibility. By the 200th cycle, the bare Zn||MnO_2 cell experiences increased voltage hysteresis and significant capacity drop (Figure 6e), reflecting deteriorated polarization and poor long-term stability. In contrast, the Fs-Zn||MnO_2 cell maintains relatively stable hysteresis and higher specific capacity. These results demonstrate the role of the nanostructured sacrificial layer in the actual operation of the battery.

3. Conclusion

This study proposes a femtosecond laser-induced sacrificial layer strategy to address surface nonuniformity and associated dendrite growth and side reaction issues in commercial-grade zinc metal for AZIBs. Upon the stripping of the Zn foil, the

fabricated nanostructures (nanopores, nanoparticles, nanocavities, and nanorims) are replaced by nearly vertical, densely packed crystal edges corresponding to the Zn(101) crystal plane. This homogenizes ion flux, ensuring uniform plating/stripping, and induces nearly (101)-oriented epitaxial growth, thereby suppressing dendrite growth. The abundant edges serve as active sites that enhance Zn ion-transport kinetics and alleviate side reactions. Accordingly, Fs-Zn symmetric cells achieve 500 h stable cycling at 1 mA cm^{-2}/1 mAh cm^{-2} (10 times longer than bare Zn), while Fs-Zn||MnO_2 full cells achieve higher capacity over 500 cycles with reduced voltage hysteresis. This scalable, non-contact femtosecond laser processing technique offers a promising approach for industrial Zn anode manufacturing for AZIBs.

Supporting Information

Supporting Information is available from the Wiley Online Library or from the author.

Acknowledgements

This research was supported by the National Key Research and Development Program of China (no. 2020YFA0715000 (L.Q.M)).

Conflict of Interest

The authors declare no conflict of interest.

Data Availability Statement

The data that support the findings of this study are available from the corresponding author upon reasonable request.

Keywords

laser materials processing, nanostructured sacrificial layer, ultrafast lasers, zinc-ion battery, zinc metal

Received: May 13, 2025
Revised: June 10, 2025
Published online: June 27, 2025

[1] Y. Dong, H. L. Hu, P. Liang, L. L. Xue, X. L. Chai, F. M. Liu, M. Yu, F. Y. Cheng, *Nat. Rev. Chem.* **2025**, *9*, 102.
[2] L. E. Blanc, D. Kundu, L. F. Nazar, *Joule* **2020**, *4*, 771.
[3] M. Iturrondobeitia, O. Akizu-Gardoki, O. Amondarain, R. Minguez, E. Lizundia, *Adv. Sustainable Syst.* **2022**, *6*, 2100308.
[4] Nantong Xinxiang Zinc Industry Co., Ltd., CN Patent 108149072, **2018**.
[5] R. Schmuch, R. Wagner, G. Horpel, T. Placke, M. Winter, *Nat. Energy* **2018**, *3*, 267.
[6] P. He, J. X. Huang, *ACS Energy Lett.* **2021**, *6*, 1990.
[7] S. D. Pu, C. Gong, Y. T. Tang, Z. Ning, J. Liu, S. Zhang, Y. Yuan, D. Melvin, S. Yang, L. Pi, J. J. Marie, B. Hu, M. Jenkins, Z. Li, B. Liu, S. C. E. Tsang, T. J. Marrow, R. C. Reed, X. Gao, P. G. Bruce, A. W. Robertson, *Adv. Mater.* **2022**, *34*, 2202552.
[8] Z. H. Yi, J. X. Liu, S. D. Tan, Z. Y. Sang, J. Mao, L. C. Yin, X. G. Liu, L. Q. Wang, F. Hou, S. X. Dou, H. M. Cheng, J. Liang, *Adv. Mater.* **2022**, *34*, 2203835.
[9] Y. X. Zhao, S. Guo, M. J. Chen, B. A. Lu, X. T. Zhang, S. Q. Liang, J. Zhou, *Nat. Commun.* **2023**, *14*, 7080.
[10] W. Xu, B. Zhang, W. Xu, G. Yao, L. Zhang, S. Lian, Q. Liu, C. Liu, R. Yuan, W. Chen, X. Qiao, K. Zhao, *Energy Storage Mater.* **2025**, *74*, 103910.
[11] M. Sun, K. Wan, Y. Huang, H. Yang, X. Zhou, C. Yan, J. Zhou, T. Qian, *Adv. Funct. Mater.* **2024**, *35*, 2417890.
[12] S. T. Lian, Z. J. Cai, M. Y. Yan, C. L. Sun, N. Y. Chai, B. M. Zhang, K. S. Yu, M. Xu, J. X. Zhu, X. L. Pan, Y. H. Dai, J. Z. Huang, B. Mai, L. Qin, W. C. Shi, Q. Q. Xin, X. Y. Chen, K. Fu, Q. Y. An, Q. Yu, L. Zhou, W. Luo, K. N. Zhao, X. W. Wang, L. Q. Mai, *Angew. Chem., Int. Ed.* **2024**, *63*, 202406292.
[13] C. Liu, W. Xu, L. Zhang, D. Zhang, W. Xu, X. Liao, W. Chen, Y. Cao, M. C. Li, C. Mei, K. Zhao, *Angew. Chem., Int. Ed.* **2024**, *63*, 202318063.
[14] Q. Jiao, X. Zhai, Z. Sun, W. Wang, S. Liu, H. Ding, W. Chu, M. Zhou, C. Wu, *Adv. Mater.* **2023**, *35*, 2300850.
[15] C. Zhao, Z. Liu, P. Wang, Z. Guo, X. Lu, Y. Zhang, N. Zhang, *Adv. Funct. Mater.* **2024**, *35*, 2411582.
[16] K. Liu, M. Sun, S. Yang, G. Gan, S. Bu, A. Zhu, D. Lin, T. Zhang, C. Luan, C. Zhi, P. Wang, B. Huang, G. Hong, W. Zhang, *Adv. Energy Mater.* **2024**, *14*, 2401479.
[17] Z. Cai, J. Wang, S. Lian, J. Chen, F. Lang, Z. Li, Q. Li, *Adv. Funct. Mater.* **2024**, https://doi.org/10.1002/adfm.202401367.
[18] J. D. Wang, Z. Cai, R. Xiao, Y. T. Ou, R. M. Zhan, Z. Yuan, Y. M. Sun, *ACS Appl. Mater. Interfaces* **2020**, *12*, 23028.
[19] J. Cao, X. Wang, S. Qian, D. Zhang, D. Luo, L. Zhang, J. Qin, X. Zhang, X. Yang, J. Lu, *Adv. Mater.* **2024**, *36*, 2410947.
[20] Y. Liu, J. Xie, Y. Ding, J. Xu, D. Huang, Y. Wang, S. Chen, Q. Hu, L. Xu, L. Yang, *Adv. Funct. Mater.* **2025**, https://doi.org/10.1002/adfm.202424526.
[21] S. K. Zhan, Z. X. Liu, F. H. Ning, X. Y. Liu, Y. Dai, S. G. Lu, Y. Y. Xia, J. Yi, *Adv. Funct. Mater.* **2025**, *35*, 2417546.
[22] L. Jiang, A. D. Wang, B. Li, T. H. Cui, Y. F. Lu, *Light Sci. Appl.* **2018**, *7*, 17134.
[23] P. Kang, Y. Yuan, F. Mo, H. Hu, *ACS Nano* **2025**, *19*, 15994.
[24] A. Gordeeva, Y. J. Hsu, I. Z. Jenei, P. H. B. Brant Carvalho, S. I. Simak, O. Andersson, U. Haussermann, *ACS Omega* **2020**, *5*, 17617.
[25] Y. Zou, X. Yang, L. Shen, Y. Su, Z. Chen, X. Gao, J. Zhou, J. Sun, *Energy Environ. Sci.* **2022**, *15*, 5017.
[26] A. Y. Vorobyev, C. L. Guo, *Opt. Express* **2006**, *14*, 2164.
[27] Y. H. Yao, Y. L. He, D. L. Qi, F. Y. Cao, J. L. Yao, P. P. Ding, C. Z. Jin, X. Y. Wu, L. Z. Deng, T. Q. Jia, F. Huang, J. Y. Liang, Z. R. Sun, S. A. Zhang, *ACS Photonics* **2021**, *8*, 738.
[28] L. V. Zhigilei, Z. B. Lin, D. S. Ivanov, *J. Phys. Chem. C* **2009**, *113*, 11892.
[29] J. X. Zheng, Q. Zhao, T. Tang, J. F. Yin, C. D. Quilty, G. D. Renderos, X. T. Liu, Y. Deng, L. Wang, D. C. Bock, C. Jaye, D. H. Zhang, E. S. Takeuchi, K. J. Takeuchi, A. C. Marschilok, L. A. Archer, *Science* **2019**, *366*, 645.
[30] W. T. Yuan, X. Y. Nie, G. Q. Ma, M. Y. Liu, Y. Y. Wang, S. G. Shen, N. Zhang, *Angew. Chem., Int. Ed.* **2023**, *62*, 202218386.
[31] Q. Li, A. Chen, D. H. Wang, Y. W. Zhao, X. Q. Wang, X. Jin, B. Xiong, C. Y. Zhi, *Nat. Commun.* **2022**, *13*, 3699.
[32] M. Zhou, S. Guo, J. Li, X. Luo, Z. Liu, T. Zhang, X. Cao, M. Long, B. Lu, A. Pan, G. Fang, J. Zhou, S. Liang, *Adv. Mater.* **2021**, *33*, 2100187.
[33] Z. Liu, Z. Guo, L. Fan, C. Zhao, A. Chen, M. Wang, M. Li, X. Lu, J. Zhang, Y. Zhang, N. Zhang, *Adv. Mater.* **2023**, *36*, 2305988.
[34] L. Jiang, Z. Xing, Y. Liu, X. Shi, L. Li, Y. Liu, B. Lu, J. Zhou, *Energy Environ. Sci.* **2025**, *18*, 3005.
[35] Q. Zhu, G. Sun, S. Qiao, D. Wang, Z. Cui, W. Zhang, J. Liu, *Adv. Mater.* **2024**, *36*, 2308577.

[36] J. Wang, J. Wang, Y. Jiang, F. Xiong, S. Tan, F. Qiao, J. Chen, Q. An, L. Mai, *Adv. Funct. Mater.* **2022**, *32*, 2113030.
[37] X. Deng, R. Zhang, K. Zhou, Z. Gao, W. He, L. Zhang, C. Han, F. Kang, B. Li, *Energy Environ. Mater.* **2022**, *6*, e12331.
[38] J. Li, H. Yang, Q. Deng, W. Li, Q. Zhang, Z. Zhang, Y. Chu, C. Yang, *Angew. Chem., Int. Ed.* **2024**, *63*, 202318042.
[39] A. Mohammadi, L. Monconduit, L. Stievano, R. Younesi, *J. Electrochem. Soc.* **2022**, *169*, 070509.
[40] H. Liu, X. B. Cheng, R. Xu, X. Q. Zhang, C. Yan, J. Q. Huang, Q. Zhang, *Adv. Energy Mater.* **2019**, *9*, 1902254.
[41] G. M. Haarberg, T. Støre, R. Tunold, *Electrochim. Acta* **2012**, *76*, 256.
[42] H. C. Shin, S. I. Pyun, S. W. Kim, M. H. Lee, *Electrochim. Acta* **2001**, *46*, 897.
[43] M. D. Levi, E. Markevich, D. Aurbach, *Electrochim. Acta* **2005**, *51*, 98.
[44] X. Tan, T. Zhao, L. Song, D. Mao, Y. Zhang, Z. Fan, H. Wang, W. Chu, *Adv. Energy Mater.* **2022**, 12.
[45] M. Zhu, Z. Fan, K. Xu, Y. Fang, W. Sun, Y. Zhu, *Adv. Funct. Mater.* **2022**, 32.
[46] Z. Y. Zhang, S. Said, K. Smith, Y. S. Zhang, G. J. He, R. Jervis, P. R. Shearing, T. S. Miller, D. J. L. Brett, *J. Mater. Chem. A* **2021**, *9*, 15355.
[47] Y. Wen, K. Yu, S. Zhan, X. Liao, Z. Zhang, X. Ran, B. Li, S. Wannapaiboon, M. Yan, *Small* **2025**, https://doi.org/10.1002/smll.202501242.
[48] J. Wang, F. Lang, Z. Cai, Q. Li, *Battery Energy* **2025**, 70022, https://doi.org/10.1002/bte2.20240107.
[49] Z. X. Wu, Y. Wang, C. Y. Zhi, *Joule* **2024**, *8*, 2442.
[50] S. D. Pu, B. K. Hu, Z. X. Li, Y. Yuan, C. Gong, Z. Y. Ning, C. Chau, S. X. Yang, S. M. Zhang, L. Q. Pi, Y. T. Tang, J. L. Yue, T. J. Marrow, X. W. Gao, P. G. Bruce, A. W. Robertson, *Joule* **2023**, *7*, 366.
[51] G. Assat, S. L. Glazier, C. Delacourt, J. M. Tarascon, *Nat. Energy* **2019**, *4*, 647.
[52] Y. Yan, X. Huang, X. Yan, F. Zhang, J. Pan, J. Wu, J. M. Moradian, *Adv. Funct. Mater.* **2025**, 2420578.

